Environmental Science Processes & Impacts

PAPER

View Article Online
View Journal

Cite this: DOI: 10.1039/d6em00196c

Iron-dependent formation and structure–property relationship of struvite precipitated from simulated wastewater

Sherif Hefney,[a] Seth Michael Koloski,[b] Philip J. Elias,[a] Damilola Tomi Awotoye,[a] Mohamed Ammar,[a] Hannah Folarin,[b] Lihua Zhang,[c] Matthijs A. van Spronsen,[d] Christie Sayes,[e] Alexander Laskin[b] and Jonas Baltrusaitis*[a]

Wastewater-derived struvite ($MgNH_4PO_4 \cdot 6H_2O$) microcrystals could replace a significant fraction of traaditional nitrogen and phosphorus fertilizers, supporting nutrient recycling and sustainability while mitigating environmental impacts such as water eutrophication and atmospheric pollution. However, phosphorus recovery is often hindered by iron interference, as iron (Fe) can strongly bind phosphate to form insoluble iron phosphate minerals, such as vivianite, through pH, redox, and organic matter dependent processes. These Fe-containing anthropogenic solids represent an unexplored source of anthropogenic iron flux into the environment. This study investigates the influence of Fe concentration on struvite formation using magnesium carbonate ($MgCO_3$) as a naturally abundant magnesium (Mg) source in simulated wastewater containing up to 500 ppm of Fe^{3+}. Iron-containing struvite (Fe-struvite) microcrystals were successfully synthesized and characterized using complementary structural and spectroscopic techniques. Up to 150 ppm Fe^{3+} precursor concentration yielded well-defined crystalline Fe-struvite, whereas higher levels resulted in amorphous phases. Low Fe^{3+} levels (up to 10 ppm) caused a lattice contraction in struvite due to limited magnesium substitution. Raman micro-spectroscopy revealed that low Fe^{3+} concentrations (<10 ppm) allowed coexistence of hydromagnesite ($Mg_5(CO_3)_4(OH)_2 \cdot 4H_2O$) with struvite, whereas at >150 ppm Fe^{3+}, only amorphous phosphate was present. Ion chromatography showed equilibrium aqueous phosphate (PO_4^{3-}) concentrations decreasing from 235 ppm to 38 ppm with increasing Fe^{3+}, while ammonium removal from solution was inhibited. X-ray fluorescence analysis indicated that at >150 ppm Fe^{3+}, an iron-rich amorphous phase with Fe : P ≈ 1 : 1.75 was produced. The findings indicate that recovered Fe-struvite can serve as an anthropogenic iron source to the environment.

Received 12th March 2026
Accepted 5th May 2026

DOI: 10.1039/d6em00196c

rsc.li/espi

Environmental significance

The environmental impact of this work is the demonstration that struvite microcrystals from wastewater can serve as a sustainable fertilizer alternative, providing not only necessary nutrients and supporting environmental remediation, but also serving as a yet unknown proxy for anthropogenic metal mobilization into the environment. It addresses phosphorus recovery challenges caused by iron interference, usually managed through costly exclusion methods. In particular, the study explores iron-containing struvite microcrystals formed from magnesium carbonate in simulated wastewater. It examines how iron influences the kinetics, structure, and chemistry of these crystals. The findings indicate that iron-enriched struvite change fundamentals of nutrient recovery and can potentially affect many natural environmental processes, such as photochemistry and photocatalysis of natural organic matter, providing new novel reactive environmental surfaces.

1 Introduction

Global demand for fertilizers is increasing in response to food security needs and the necessity to preserve the natural phosphate rock resources, while the paradigm governing wastewater treatment is shifting from nutrient immobilization and disposal to recovery and reuse.[1,2] Wastewater can thus be considered a significant secondary source of essential nutrients.[3] Phosphorus (P) and nitrogen (N) are abundant in raw

[a]Department of Chemical and Biomolecular Engineering, Lehigh University, 124 E. Morton St., Bethlehem, PA 18015, USA. E-mail: job314@lehigh.edu
[b]Department of Chemistry, Purdue University, West Lafayette, Indiana 47907, USA
[c]Brookhaven National Laboratory Center for Functional Nanomaterials, Bldg. 735, Upton, New York 11973-5000, USA
[d]Harwell Science and Innovation Campus, Diamond Light Source Ltd, Didcot, Oxfordshire, OX11 0DE, UK
[e]Department of Environmental Science, Baylor University, Waco, Texas 76798-7266, USA

wastewater but are typically removed during conventional treatment processes. Nitrogen is present predominantly as ammonium (NH_4^+) due to the hydrolysis of urea and proteins, while phosphorus occurs in various orthophosphate and polyphosphate forms.[4,5] The overall chemistry of wastewater is very complex due to the presence of metal ions, particularly ferric (Fe^{3+}) and ferrous (Fe^{2+}) ions. Iron ions enter treatment systems either naturally through influent at concentrations up to 10 ppm or intentionally as coagulants containing ferric or ferrous salts.[6] Phosphorus readily binds to iron to form stable, low-solubility iron phosphate minerals or strongly adsorbed surface complexes within treatment sludges.[7] The omnipresence of iron within wastewater treatment infrastructure, whether from influent or from iron salts used in wastewater treatment, presents a significant barrier to conventional nutrient recovery.

In struvite ($MgNH_4PO_4 \cdot 6H_2O$) crystallization processes, which are widely explored for simultaneous N and P recovery, metal ions, particularly Fe^{3+}, act as effective inhibitors due to thermodynamically favored phosphate complexation.[8–12] When iron is available, it competes with magnesium for phosphate-binding sites, promoting precipitation of stable, often amorphous iron phosphate phases in addition to crystalline struvite.[6] Wang *et al.* studied the hydrothermal treatment (HT) of anaerobically digested, iron-rich sludge and demonstrated that vivianite ($Fe_3(PO_4)_2 \cdot 8H_2O$) was the dominant product even at low HT temperatures.[10] At higher temperatures or extended residence times, strengite ($FePO_4 \cdot 2H_2O$) was favored thermodynamically, primarily due to the thermally driven auto-oxidation of ferrous ions. During subsequent nutrient recovery *via* Mg^{2+} addition and pH adjustment to 8.0, metal ions, such as Fe, Al, and Ca, acted as kinetic inhibitors, suppressing the growth of specific struvite crystal faces (002 and 004) and reducing overall crystal purity.[13,14] The relative abundance of struvite and vivianite phases was governed by the initial Fe : Mg molar ratio and solution pH. Struvite crystallization was particularly sensitive to acidogenic conditions induced by HT treatment and was significantly inhibited by iron. In contrast, vivianite formation was reinforced by both chemical and microbial reduction, making it the dominant phosphorus sink in iron-rich sewage sludge.[15] Guan *et al.* showed that increasing solution pH/hydroxide (OH^-) concentrations drives the spontaneous hydrolysis of transition-metal cations (such as Fe^{3+}).[16] Under the basic conditions (pH 8.5–10.0), the precipitation of insoluble metal hydroxides, such as $Fe(OH)_3$, takes place. Those hydroxide phases can form concurrently with the struvite. Although this co-precipitation represents a parallel reaction pathway, it involves complex surface-mediated interactions. Metal hydroxide flocs, characterized by high surface areas and variable surface charges, mediate adsorption of orthophosphate ions (PO_4^{3-}),[6,16] leading to formation of amorphous metal-phosphate aggregates. As a result, the recovered solid phase is a heterogeneous composite in which struvite is interdispersed with amorphous hydroxide and phosphate precipitates. At very high pH levels (>10.5), the precipitated solids may undergo a further transition toward magnesium hydroxide formation ($Mg(OH)_2$), which competes with the struvite crystallization and alters the resulting mineralogical composition of the precipitate.[16] Yan and Shih studied the inhibitory effect of Fe^{3+} ions on struvite crystallization[8] and showed that the spontaneous formation of amorphous ferric hydroxyl–phosphate complexes effectively sequesters bioavailable phosphorus.[8] Consequently, solution supersaturation with respect to struvite is substantially reduced, suppressing nucleation. Rietveld refinement of the recovered solids demonstrated that ferric ions do not perturb the internal lattice parameters of struvite, indicating that inhibition is governed primarily by surface adsorption rather than lattice substitution. Morphologically, the presence of ferric precipitates modified the characteristic needle-like struvite microcrystals into irregular, roughened aggregates with significant surface cracking. These iron-containing solid particles act as heterogeneous nuclei, disrupting the preferred crystallographic growth along the longitudinal axis.[8]

Struvite crystallization requires an equimolar ratio of magnesium (Mg^{2+}), ammonium (NH_4^+), and phosphate (PO_4^{3-}). Wastewater is typically magnesium-deficient, and conventional recovery strategies therefore rely on the addition of soluble magnesium chloride ($MgCl_2$) or magnesium sulfate ($MgSO_4$).[17,18] Alternative approaches have recently explored the use of low-solubility magnesium precursors, such as magnesium oxide or magnesium carbonate.[19,20] Importantly, naturally occurring Mg-bearing minerals employed in struvite synthesis, such as periclase (MgO) and magnesite ($MgCO_3$), commonly contain iron as an impurity. In periclase, iron is particularly common because Fe^{2+} can isovalently substitute for Mg^{2+}, forming mixed FeO–MgO crystals with iron mass fractions up to 13%.[21] In mantle-derived rocks, natural FeO–MgO minerals span nearly the full compositional range between FeO to MgO phases. However, the mass fraction of iron in natural magnesite is lower, about 1%.[22] Despite this variability, the mechanisms by which iron is incorporated into the struvite lattice and how this affects struvite solubility have been a subject of significant interest and remain poorly constrained.[23]

In this study, we investigate the formation of iron-containing struvite using simulated wastewater solutions derived from a low-solubility magnesium source ($MgCO_3$). The systems span Fe^{3+} concentrations from 10 ppm, typical of wastewater, to 200 ppm, with selected cases extended to 500 ppm to reflect post-coagulation scenarios. This approach enables systematic evaluation of the structural, chemical, and surface properties of Fe-containing struvite formed under environmentally relevant conditions. While the macroscopic thermodynamic preference for iron-phosphate precipitation is well established, this work focuses on resolving the microstructural transitions that accompany increasing iron content. Specifically, the study aims to determine the threshold concentration at which intra-lattice iron incorporation gives way to amorphous phase segregation. Furthermore, the co-precipitation approach is employed to approximate the dynamic dissolution–recrystallization processes inherent to wastewater treatment systems. Although these processes may occur sequentially in practice, fluctuations in solution pH can induce partial dissolution of existing mineral phases, followed by recrystallization in an iron-containing medium. Under such conditions, competitive

interactions between the reforming struvite lattice and Fe^{3+} ions can be effectively captured by the co-precipitation experiment. Consequently, this methodology enables assessment of structural evolution across conditions ranging from trace-level recovery (≤10 ppm Fe^{3+}) to high-loading interference scenarios (≤500 ppm Fe^{3+}), thereby establishing a baseline for the structural integrity of recovered nutrients under chemically dynamic environments.

2 Experimental and methods

2.1 Materials and synthesis

$MgCO_3$ powder (99%+, Thermo Scientific Chemicals, USA), $NH_4H_2PO_4$ (99.9%+, Fisher Scientific, USA) and $Fe(NO_3)_3 \cdot 9H_2O$ (99.9%+, Fisher Scientific, USA) were used as received. An 18.2 MΩ cm^{-1} DI water (Millipore, Bedford, MA, USA) was used for dilution in all cases.

Struvite ($NH_4MgPO_4 \cdot 6H_2O$) was synthesized through a solution-based precipitation method using monobasic ammonium phosphate (MAP, $NH_4H_2PO_4$) selected for its high solubility (approximately 40 g/100 mL)[24] as the nitrogen and phosphorus source. In addition, hydrated magnesium carbonate ($MgCO_3 \cdot xH_2O$) which is characterized by its low solubility product (log $K_{sp} = -37.08$),[25] was utilized as the magnesium precursor A 1000 ppm (in total, at the end) magnesium suspension was prepared by dispersing 0.5 g of $MgCO_3$ in 250 mL of deionized water under magnetic stirring at 300 rpm. This concentration was previously shown to result in maximum NH_4^+ removal from simulated wastewater solutions.[19] Separately, a 600 ppm (in total, at the end) MAP solution was prepared by dissolving 0.3 g of MAP in 250 mL of deionized water. Once dissolution was complete, the MAP solution was rapidly added to the $MgCO_3$ suspension under continuous stirring. This rapid addition, rather than gradual dripping, was intended to induce a broad particle-size distribution and favor the formation of well-grown crystals. The reaction mixture was stirred for 10 min, followed by 60 min of aging to allow for further crystal growth. The resulting precipitate was collected by vacuum filtration using a Büchner funnel and dried under vacuum until a constant mass was obtained. The overall reaction for struvite formation is given in eqn (1).

$$NH_4^+ + Mg^{2+} + PO_4^{3-} + 6H_2O \rightarrow NH_4MgPO_4 \cdot 6H_2O(s) \quad (1)$$

where Mg^{2+} originates in the vicinity of the complex solid–liquid equilibrium at $MgCO_3$ particle surfaces. During all reactions, pH was not adjusted but measured, except for 500 Fe-struvite, where pH was increased using NaOH to 9. Previous results showed that the use of alkaline solids, such as MgO and $MgCO_3$, leads to facile hydroxylation, with the resulting pH increase sufficient to drive struvite formation.[26]

Fe-containing struvite was synthesized following a method similar to that of pure struvite, with the addition of ferric nitrate nonahydrate ($Fe(NO_3)_3 \cdot 9H_2O$). Three aqueous stocks were prepared of 1000 ppm of $MgCO_3$ suspension, 600 ppm of MAP, and a $Fe(NO_3)_3 \cdot 9H_2O$ solution containing the desired Fe^{3+} concentrations (x = 6, 10, 20, 50, 100, 150, 200, and 500 ppm). These samples are referred to as 'x ppm Fe-struvite', where x is the concentration of Fe^{3+} in the precursor solution. To minimize $Fe(OH)_3$ precipitation and to enhance the likelihood of Fe^{3+} incorporation into struvite microcrystals, the Fe^{3+} solution was added to the magnesium/ammonium suspension under continuous stirring. Immediately after the addition of the MAP solution, the ferric nitrate solution was introduced. The mixture was stirred for 10 min and then left undisturbed for 60 min to allow the formed crystal growth. The resulting precipitate was collected using a Büchner funnel and dried under vacuum.

2.2 Chemical characterization

X-ray diffraction (XRD) measurements were performed on a PANalytical Empyrean diffractometer using Cu Kα radiation (λ = 1.5406 Å), operated at 45 kV and 40 mA. The incident beam was conditioned with a 1/4° divergence slit and 0.04 rad Soller slits. Data were collected over the 5–50° 2θ range using a PIXcel3D detector in continuous scanning mode with a counting time of 13.77 s per step. Phase identification and Rietveld refinement were performed using the Profex (BGMN) software package. To ensure structural accuracy, standard reference files were sourced from the International Centre for Diffraction Data (ICDD) for struvite (01-075-0674) and the Crystallography Open Database (COD) for hydromagnesite (9007620).[27,28]

Relative elemental abundances of the Fe-struvite powders were determined by energy-dispersive X-ray fluorescence (ED-XRF) spectroscopy using a Malvern Panalytical Epsilon 4 benchtop spectrometer. Approximately 1–2 g of loose powder was loaded into nylon sample cups, each covered with a 4.0 μm polypropylene support film, and placed in the instrument sample holder. Polypropylene was selected for its low X-ray attenuation for light elements and its minimal inorganic background contribution relative to other common polymer films, thereby improving the accuracy of quantitative light-element analysis. Measurements were conducted under vacuum using the standard instrument configuration. To obtain broad elemental coverage and minimize matrix-related interferences, six measurement modes were used, including low- and high-energy settings with different excitation voltages and tube currents, primary beam filters, and helium purging. Triplicate measurements were acquired to ensure reproducibility and provide accurate statistics for quantitation. Elemental spectra were processed using Omnian software for spectral deconvolution and background correction, and trace signals attributable to non-sample contributions were excluded.

Speciation of iron in bulk Fe-struvite powders was investigated using synchrotron-based X-ray absorption near-edge structure (XANES) spectroscopy at the Fe L-edge (695–720 eV). Complementary measurements were performed at the P K-edge (2120–2200 eV). Experiments were conducted at the Diamond Light Source, beamline B07B (Versatile Soft X-ray, VerSoX), Oxfordshire, United Kingdom.[29] For the measurements, a 600-lines-per-mm grating was used set to a c_{ff} of 1.4 and exit slits to 0.05 mm in the dispersive direction. Struvite powders with varying iron contents, along with reference materials, were individually pressed onto indium foil and mounted in the

XANES analysis chamber. The chamber was evacuated to high vacuum and backfilled with helium to a pressure of several mbar to minimize artefacts due to charging. The monochromated X-ray beam was scanned across the respective edge and (at least) two points were measured for each sample/edge combination, and the total electron and total fluorescence yield were collected for the determination of iron speciation. Two major peaks (707.8 and 709.5 eV) were used to determine any relative contributions of Fe(II) and Fe(III) within the samples, following the approach described by Moffet *et al.*[30] Due to experimental conditions, these absolute energy positions did not exactly align with our spectra; therefore, the peak positions were shifted consistently to match the data while preserving the energy separation defined in the reference.

Ion chromatography (IC) was performed using a Metrohm Eco 925 system (Herisau, Switzerland). Anionic and cationic separations were achieved using Metrosep A Supp 5 and Metrosep C 4 analytical columns, respectively, each equipped with the corresponding guard columns. Eluted species were monitored by conductivity detection. For cation analysis, an eluent composed of dipicolinic acid (1.75 nM/0.7 mM) was used. Conversely, anion separation was performed using a mobile phase of 3.2 mM Na_2CO_3 and 1.0 mM $NaHCO_3$. MagIC Net software was used for instrument control and data acquisition. Supernatants were separated into three groups for anion, cation, and total Fe analyses and subsequently filtered. For total Fe, the filtered supernatants were acidified with 5 M HCl to pH less than 2 to preserve dissolved species prior to colorimetric quantification utilizing the 1,10-phenanthroline assay.[31,32]

High-resolution transmission electron microscopy (HRTEM) images and the high-angle annular dark-field scanning TEM (HAADF-STEM) maps were data were acquired using a Thermo Fisher Talos 200X 200 keV high-resolution analytical scanning/transmission electron microscope equipped with a four-quadrant energy-dispersive X-ray spectrometer for elemental and compositional mapping.

Confocal Raman micro-spectroscopy was performed using a WITec alpha300R system with a 532 nm excitation laser. Measurements were conducted using a Zeiss 100× or 20× objectives and a 600 g mm^{-1} grating, across a spectral range of 500–4000 cm^{-1}. The system was calibrated using a silicon wafer to ensure the spectral resolution of 2 cm^{-1}. Spatial heterogeneity was evaluated through 2D spectral mapping in the *x*-*y* plane.

X-ray photoelectron spectroscopy (XPS) was performed on a SPECS instrument equipped with a μ-FOCUS 600 X-ray monochromator, operating in UHV mode. Al Kα radiation was used with an X-ray beam energy of 1486.7 eV and a power of 100 W. Spectra were acquired using a PHOIBOS 1D-DLD hemispherical analyzer with an energy resolution of 0.85 eV. Survey spectra were collected using a pass energy of 100 eV, a step size of 1 eV, and a dwell time of 100 ms. High-resolution scans were acquired at a pass energy of 20 eV, a step size of 0.1 eV, and a dwell time of 1 s. Quantification was performed using Scofield relative sensitivity factors (RSF).[33] The inelastically scattered background was subtracted using Shirley's method.[34] CasaXPS v2.3.6rev1.0Q was employed for all data processing tasks.[35] To mitigate surface charging effects inherent to non-conducting samples, a low-energy electron flood gun was utilized for charge compensation during spectral acquisition. Furthermore, all binding energies were calibrated by referencing the adventitious carbon C 1s peak to 285 eV.

Surface charge properties of struvite and Fe-struvite were evaluated *via* electrophoretic light scattering (ELS) using an Anton Paar Lightesizer 701 instrument. To ensure constant ionic strength, samples were dispersed in a 10 mM NaCl background electrolyte. Measurements were conducted at 25 °C using a folded capillary cell (Omega cuvette). Each reported value represents the average of three independent measurements, with each measurement comprising 25 runs to ensure statistical reliability.

2.3 Quantum chemical calculations

All first-principles calculations were performed using the CRYSTAL23 code, which uses a periodic *ab initio* approach based on localized Gaussian-type orbitals within the Kohn–Sham density functional theory (DFT).[36] The PBEsol0 hybrid functional was used to describe electron exchange and correlation, and all-electron Gaussian basis sets optimized for solid-state systems were employed. Reciprocal-space integration utilized a Monkhorst–Pack grid (6 × 6 × 6 with 64 *k*-points in the irreducible Brillouin zone), ensuring total-energy convergence to within 10^{-11} Ha. The self-consistent field (SCF) convergence threshold for the energy change was set to 1.0 × 10^{-7} Ha. Dispersion interactions were treated using the DFT-D3(BJ) correction scheme of Grimme's method.[37,38] The basis set was pob-TZVP-rev2.[39] Vibrational frequencies were computed at the Γ point within the harmonic approximation. Raman intensities were evaluated within the harmonic framework using the coupled-perturbed Kohn–Sham (CPKS) method as implemented in CRYSTAL23.[40–42] All calculations were carried out under periodic boundary conditions of a fully optimized unit cell and atomic positions of the struvite crystal at 0 K.[43]

3 Results and discussion

3.1 Fe-struvite formation kinetic measurements

Time-resolved concentration profiles of Mg^{2+}, NH_4^+, PO_4^{3-} and total Fe during Fe-struvite synthesis are shown in Fig. 1. The equilibrium concentration of Mg^{2+} ions increased with time as Mg^{2+} was released from the low solubility $MgCO_3$ precursor, reaching a saturation plateau within the first 10 min. This indicates that the subsequent 60 min static aging period exerts a negligible influence on solution equilibrium. Notably, increasing Fe^{3+} concentration resulted in higher Mg^{2+} concentration in solution, suggesting inhibited incorporation of magnesium into the solid struvite phase. During the active stirring phase, NH_4^+ concentration in solution also is higher for the higher Fe^{3+}concentrations, whereas PO_4^{3-} concentrations decreased rapidly with increasing Fe^{3+}, as shown in Fig. 1b–c. This behavior has important implications for the composition of the resulting microcrystals, which incorporate more

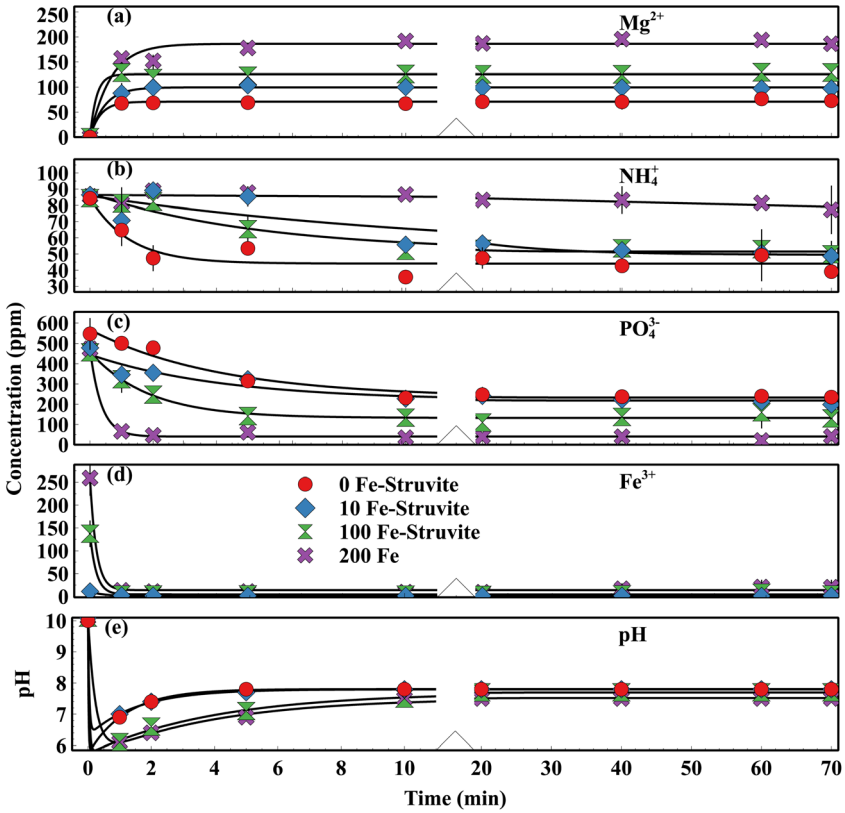

Fig. 1 Time resolved (a) Mg^{2+} (b) NH_4^+ (c) PO_4^{3-}, (d) total Fe ion concentration profiles and (e) the resulting solution pH during Fe-struvite synthesis using 1000 ppm $MgCO_3$ and 600 ppm MAP.

phosphate but less ammonium in the presence of iron. The equilibrium PO_4^{3-} concentrations in the supernatant were approximately 235 ppm for Fe-free struvite and 38 ppm for the 200 ppm Fe-struvite microcrystals. Fig. 1d shows that the total iron concentration in solution decreased to near zero almost immediately, indicating rapid incorporation of iron into the solid phase. Solution pH reached equilibrium within 10 min, increasing from an initial value of approximately 6.0 to a steady-state range of 7.5–7.8 (Fig. 1e), which is thermodynamically favorable for struvite crystallization, consistent with previous studies.[44]

To further examine how added Fe^{3+} affects struvite synthesis kinetics, the transient concentration of dissolved phosphate (PO_4^{3-} mg L^{-1} solution) shown in Fig. 1c was analyzed. The kinetic data were obtained by fitting the curves in Fig. 1c curves to a pseudo-second-order kinetic model. Linearized plots of t/q_t *versus* t were constructed, where q_t is the transient removal capacity of PO_4^{3-}. From the slope and intercept of these linear fits, the equilibrium phosphate removal capacity q_e (PO_4^{3-}) and the pseudo-second-order rate constant k_2 were calculated.[23] For k_2, the value represents the pseudo-second-order rate constant, which assumes that the rate of PO_4^{3-} removal is proportional to the square of the available unreacted capacity. The resulting kinetic parameters are summarized in Table 1. Specifically, the q_e derived from the linearized plots for 0, 10, 100, and 200 ppm Fe^{3+} precursor solutions were 0.598, 0.585, 0.694, and 0.930 PO_4^{3-} mg L^{-1}, respectively (Fig. 2a). These results indicate no significant change in the equilibrium phosphate removal at low Fe additions, whereas higher Fe concentrations lead to a measurable increase in PO_4^{3-} removal at equilibrium. In contrast, k_2 increased only slightly from 0.552 L mg^{-1} min^{-1} at Fe-free to 0.801 L mg^{-1} min^{-1} at 10 ppm Fe^{3+}, but increased by more than an order of magnitude to 6.04 L mg^{-1} min^{-1} and 8.83 L mg^{-1} min^{-1} at 100 ppm and 200 ppm Fe^{3+}, respectively. Given that lattice substitution is proposed to occur only up to ~10 ppm Fe^{3+}, as indicated by the XRD data shown in Fig. 4b, the sharp increase in k_2 at higher Fe^{3+} concentrations suggests formation of secondary phases. In particular, because ammonium concentrations increase in solution with increasing Fe^{3+} addition (Fig. 2b), while phosphate is concurrently consumed, phosphate removal is more likely governed by the formation of iron phosphate species rather than struvite. Overall, the pseudo-second-order model provides an excellent description of the system, with good agreement (R^2 > 0.99) across all iron

Table 1 The calculated q_e (O_4^{3-} mg L^{-1}) and k_2 (L mg^{-1} min^{-1}) for PO_4^{3-} adsorption using 0, 10, 100, and 200 ppm Fe added

Fe^{3+} added (ppm)	q_e (PO_4^{3-} mg L^{-1})	k_2 (L $mg^{-1}min^{-1}$)
0	0.60	0.55
10	0.59	0.80
100	0.69	6.04
200	0.93	8.83

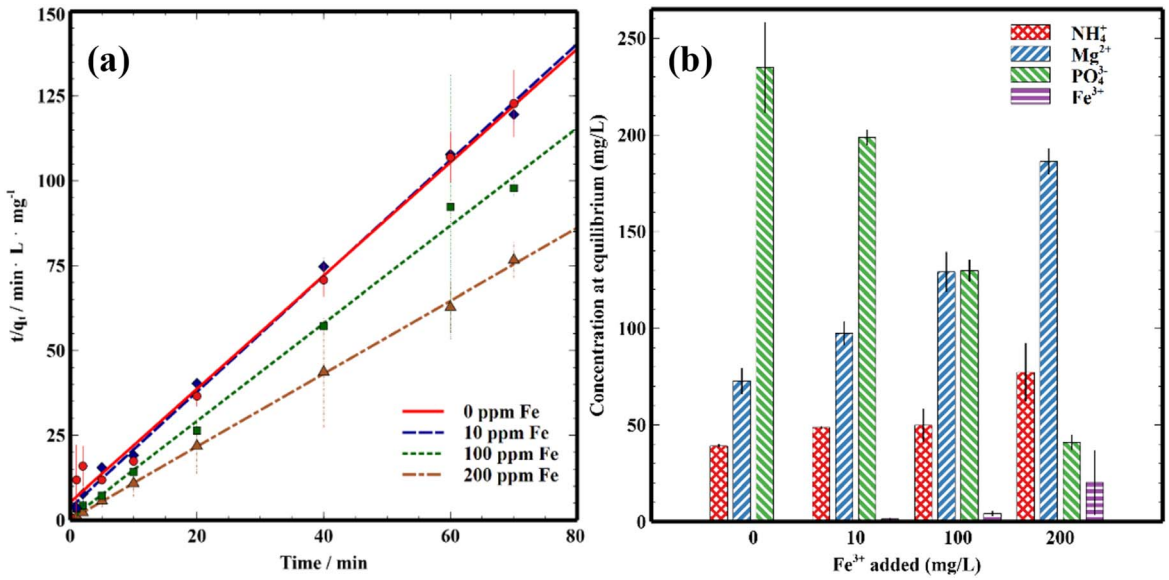

Fig. 2 (a) Linearized pseudo-second-order kinetic plot. (b) Equilibrium concentrations of residual ions, ammonium, magnesium, phosphate, and iron ions.

additions. Overall, the pseudo-second-order model provides an excellent description of the system, with good agreement across all Fe^{3+} concentrations.

3.2 XRF compositional analysis of Fe-struvite

The bulk atomic composition of Fe-struvite and the resulting molar ratios determined by XRF are shown in Fig. 3, indicating a competitive displacement mechanism between iron and magnesium. As Fe^{3+} concentration in the precursor solution increases from zero to 150 ppm, the atomic percent of iron in the solid product increases and approaches saturation at higher concentrations. Concurrently, Mg and P concentrations decrease steadily in the solid phase, in agreement with the IC results discussed later. XRF analysis further shows that while the Mg/P ratio decreases and plateaus in the 150–500 ppm Fe-struvite samples, the Fe/P ratio continues to increase, reaching values close to 10 in the 500 ppm Fe-struvite sample. This trend indicates that iron exceeds the available phosphorus and therefore co-precipitates with struvite as a secondary non-phosphate phase, such as iron oxides or hydroxides. A compositional crossover is observed starting at 50 ppm Fe-struvite, where iron becomes the dominant cation, with an Fe/Mg ratio of 1.6. As additional Fe^{3+} is introduced into the precursor solution, iron increasingly dominates the solid composition. While the Fe/P atomic ratio continues to rise, the Mg/P ratio decreases and stabilizes at approximately 0.4, indicating strong yet incomplete displacement of magnesium by iron within the system.

These observations suggest that while the original $Mg-PO_4$ framework of the struvite lattice is disrupted, a substantial

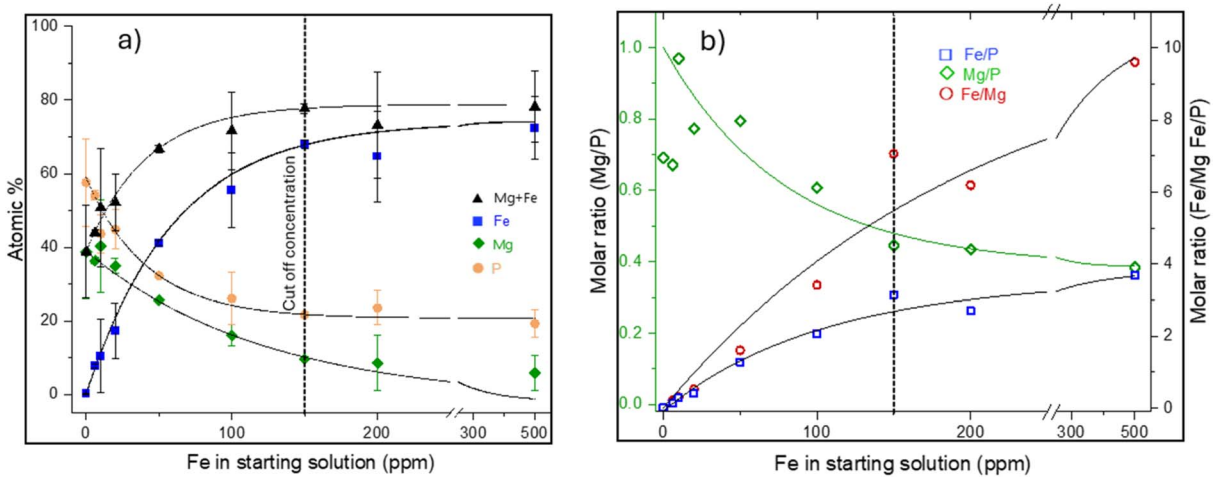

Fig. 3 (a) Atomic composition (%) of Fe, Mg, and P elements based on XRF analysis, with a line that determines the cutoff concentration when crystalline struvite does not form, (b) molar ratios of Fe/P, Mg/P, and Fe/Mg.

fraction of phosphate is retained and incorporated into an iron-rich amorphous phosphate phase in 50 and 100 ppm Fe-struvite samples. In ≥150 ppm Fe-struvite samples, the Fe/P ratio exceeds 3, indicating significant deviation from the stoichiometry expected for pure iron phosphate phases. At the highest iron loading (500 ppm Fe-struvite), the Fe/P ratio approaches 4, confirming that the resulting solid product is not composed solely of iron phosphate. Instead, available phosphate is consumed to form iron phosphate domains, while excess iron precipitates as iron (oxy)hydroxide phases such as FeOOH or $Fe(OH)_3$.

3.3 X-ray diffraction (XRD) analysis of Fe-struvite microcrystals

XRD analysis is carried out to investigate the structural properties of struvite synthesized from $MgCO_3$ in the presence of varying Fe^{3+} concentrations, as shown in Fig. 4. The struvite phase was confirmed for microcrystals synthesized with Fe^{3+} concentrations up to 150 ppm, with no crystalline iron-containing minerals detected. Above this precursor concentration, the characteristic crystalline struvite peaks disappeared. Furthermore, the XRD patterns of the 100 ppm and 150 ppm Fe-struvite microcrystals showed increased background levels and peak broadening compared to lower Fe^{3+} concentrations, as shown in Fig. 4a. This suggests the presence of a low crystallinity or amorphous solid phase. This observation is consistent with recent reports of amorphous iron phosphate intermediates formed during vivianite formation.[45] A small albeit systematic shift to higher diffraction angles was observed from pure struvite to 10 ppm Fe-struvite, as illustrated in Fig. 4b for the (111) plane, reflecting changes in interplanar spacing (*d*-spacing). According to Bragg's law, a shift to higher 2θ values corresponds to a decrease in *d*-spacing, indicating lattice contraction.[46,47] Accordingly, lattice contraction is evident for the 6 and 10 ppm Fe-struvite. This contraction is likely associated with ionic substitution, in which Fe^{3+} ions (ionic radius ≈0.645 Å)[48] partially replace Mg^{2+} ions (ionic radius ≈ 0.72 Å[49]) at crystallographic sites. The difference in ionic radii (~10.4%) satisfies one of the criteria for substitution (<15% difference in the radii).[50] However, the charge difference between Mg^{2+} and Fe^{3+} suggests that substitution remains limited, consistent with the maximum lattice shift observed for 10 ppm Fe-struvite. Support of this partial substitution of Fe is provided by previous reports of ammonium iron (II, III) phosphate phases.[51] An additional contribution to the observed peak shifts may arise from microstrain associated with inhomogeneous dopant distribution, defect formation, or incomplete structural accommodation of substituted ions.[52]

The structural properties of Fe-struvite synthesized using $MgCO_3$ were further evaluated by Rietveld refinement of powder XRD data, as shown in Fig. 5a. The Rietveld-refined XRD patterns are presented for 0, 6, 10, and 100 ppm Fe-struvite microcrystals. In all cases, the dominant crystalline phase corresponded to orthorhombic struvite (space group $Pmn2_1$).[53] A peak observed at 9.2° during the refinement is attributed to the cubic hydrated magnesium carbonate (hydromagnesite) phase, corresponding to the (100) plane.[54] This suggests that not all hydromagnesite reacted to form struvite in the Fe-free microcrystals. Notably, as Fe^{3+} concentration increased, this peak gradually disappeared, suggesting enhanced dissolution of the Mg-bearing precursor. This may be attributed to the acidic nature of ferric nitrate nonahydrate.

Pronounced differences were also observed in the spectral background. Specifically, the Rietveld-refined XRD patterns of the 100 ppm Fe-struvite microcrystals exhibit elevated background intensity relative to those at lower Fe^{3+} concentrations.

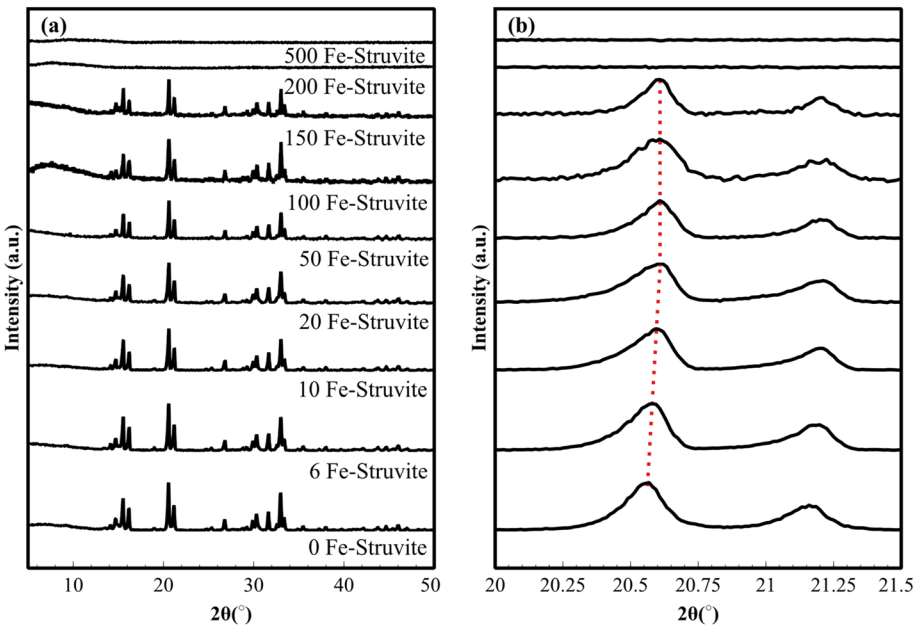

Fig. 4 (a) XRD patterns of struvite synthesized from $MgCO_3$ in the presence of various concentrations of Fe^{+3} ions, (b) observed shift in the (111) plane.

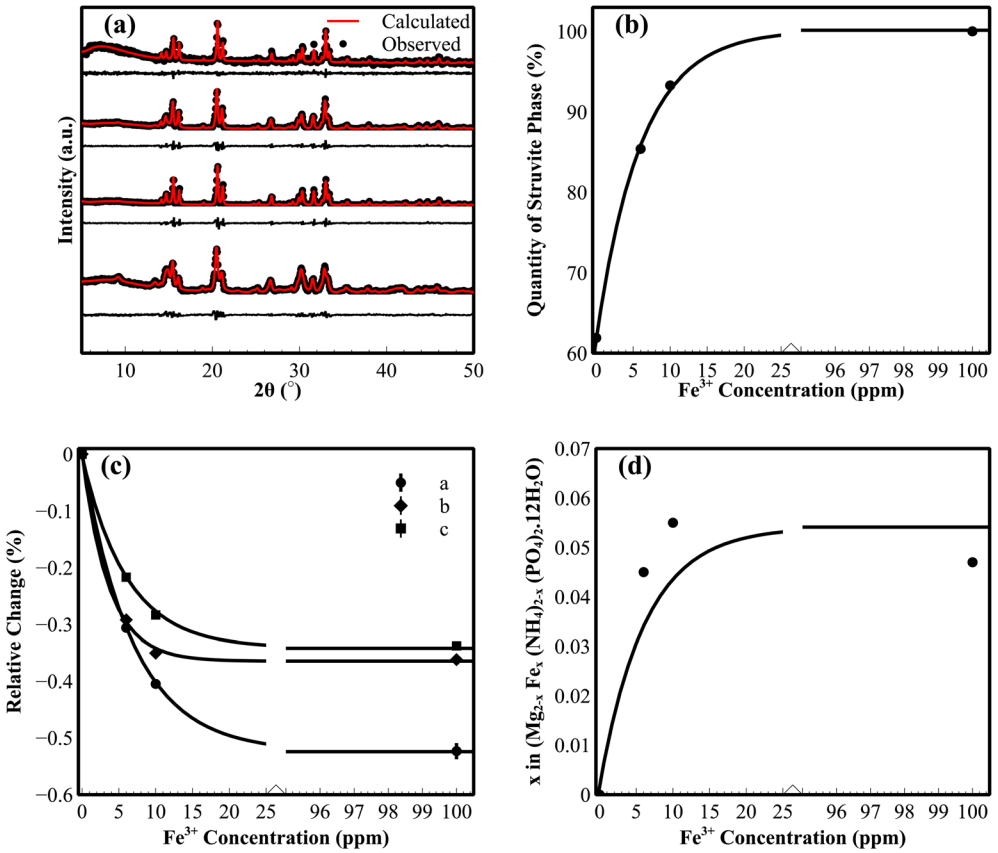

Fig. 5 (a) Rietveld refined XRD patterns and (b) the resulting quantification of struvite phase, (c) the lattice contraction with iron loading (d) molar substitution fraction of iron in struvite lattice.

This indicates the formation of a poorly crystalline or amorphous secondary phase that does not contribute to Bragg reflections. Consistent with this observation, Fig. 5b shows that the fraction of crystalline struvite increases from 62% to 100% as Fe^{3+} concentration increases from 0 ppm to 100 ppm. Therefore, the secondary phase is not associated with struvite and may instead be an amorphous iron phosphate.

In Fig. 5c and Table 2, the struvite lattice parameters decrease with increasing Fe content, except for the b-parameter, which decreases only up to 10 Fe-struvite.

The refinement converged to a substitution quantity of Fe/Mg at maximum in the range of 5–6% per double unit cell used in the fit, as shown in Fig. 5d and the substitution can be represented by eqn (6). This value indicated a defect-type formation rather than separate crystalline phase formation, such as K-struvite or Na-struvite[52,55–57]. While the exact defect formation mechanism cannot be inferred from the XRD data alone, the constraint during the refinement was enforced of Fe^{3+} + Mg^{2+} unity and the lattice NH_4^+ vacancy complementing Fe^{3+} incorporation to preserve the charge neutrality described by eqn (2)–(4).

$$Occ_{Fe^{3+}} + Occ_{Mg^{2+}} = 1 \quad (2)$$

where Occ denotes the fractional site occupancy, thus, $Occ_{Fe^{3+}}$ and $Occ_{Mg^{2+}}$ represent the fractional occupancies of the substituted ferric ions and the host magnesium ions, respectively

$$Occ_{NH_4^+} = Occ_{Mg^{2+}} \quad (3)$$

$$\left[Fe_{Mg}^{\bullet}\right] = \left[V'_{NH_4}\right] \quad (4)$$

where the square brackets denote defect concentrations. In standard Kröger–Vink notation, $Fe_{Mg}^{\bullet}$ represents Fe^{3+} ion substituting Mg^{2+} lattice site and therefore yielding one effective positive charge. Conversely, V'_{NH_4} is the ammonium lattice vacancy and therefore yielding one effective negative charge.

The standard Kröger–Vink notation for the proposed aliovalent substitution observed in Fe-struvite can then be written as eqn (5)

Table 2 Lattice parameters resulting from Rietveld refinement of struvite microcrystals synthesized in the presence of various amounts of Fe^{3+} ions

Microcrystal	a (Å)	±	b (Å)	±	c (Å)	±
0 Fe-struvite	6.9895	0.0009	6.1624	0.0008	11.2520	0.0010
6 Fe-struvite	6.9681	0.0007	6.1444	0.0005	11.2276	0.0009
10 Fe-struvite	6.9613	0.0004	6.1406	0.0003	11.2201	0.0006
100 Fe-struvite	6.9529	0.0010	6.1401	0.0006	11.2140	0.0010

$$Fe^{3+} + Mg_{Mg}^{\times} + (NH_4)_{NH_4}^{\times} \rightarrow Fe_{Mg}^{\bullet} + V'_{NH_4} + Mg^{2+} + NH_4^{+} \quad (5)$$

where $Mg_{Mg}^{\times}$ and $(NH_4)_{NH_4}^{\times}$ denote magnesium and ammonium ions residing on their respective regular lattice sites with a neutral effective charge.

Hence, the generalized equation illustrating Fe-struvite formation at concentrations of Fe^{3+} lower than 100 ppm might be written as eqn (6).

$$(1-x)NH_4^{+} + (1-x)Mg^{2+} + xFe^{3+} + PO_4^{3-} + 6H_2O \rightarrow (NH_4)_{(1-x)}Mg_{(1-x)}Fe_xPO_4\cdot 6H_2O(s) \quad (6)$$

where x corresponds to the molar fraction of Fe^{3+} substituting for Mg^{2+} in the struvite lattice.

The results in Fig. 5 suggest that struvite synthesis using $MgCO_3$ proceeds *via* a heterogeneous mechanism and is initially localized at the solid–liquid interface. This surface-limited reaction pathway delays the full availability of Mg^{2+} ions and results in non-uniform struvite nucleation. Such reaction conditions may promote the formation of structural defects within the struvite lattice. One type of these defects may involve localized substitutional sites at which Fe^{3+} can be more readily incorporated. Limited diffusion of Mg^{2+} ions and the presence of $MgCO_3$ at the interface further destabilizes the growth environment, potentially leading to increased defect formation and crystallite anisotropy. During the reaction, carbonate ions (CO_3^{2-}) released from $MgCO_3$ may be converted to carbon dioxide (CO_2) under the acidic conditions introduced by MAP, in addition to ferric nitrate.[58–60] The generated CO_2 can further escape from the aqueous system and drive the continuous dissolution of the precursor, thereby buffering the local acidity.[60,61] This system represents a dynamic equilibrium between carbonate dissolution, carbon dioxide evolution, and re-acidification, creating a chemically fluctuating environment that strongly influences the kinetics and pathways of struvite precipitation. Acidic conditions favor the continued dissolution of $MgCO_3$, increase Mg^{2+} concentrations in solution, and may destabilize nascent struvite microcrystals, thereby promoting additional defect formation. However, these processes are most pronounced during the initial few minutes of the reaction, after which pH increases as CO_2 escapes from the system.

3.4 XANES analysis of Fe-struvite microcrystals

To elucidate the local coordination environment and oxidation states of iron and phosphorus in Fe-struvite, Fe L-edge and P K-edge XANES spectra were collected for the resulting Fe-struvite microcrystals, as shown in Fig. 6a–b. The P K-edge spectra of Fe-free struvite exhibits a distinct absorption peak at 2139 eV. As the Fe^{3+} precursor concentrations increased from 100 ppm to 500 ppm, this peak exhibited a systematic blue shift toward higher energy (from 2139 eV to 2140 eV), accompanied by peak broadening and the formation of a broad pre-edge feature at ~2135 eV. This pre-edge feature has previously been assigned to the amorphous PO_4^{3-} associated with iron phosphate compounds.[62] Furthermore, at high Fe^{3+} loadings (200–500 ppm), the overall spectral profile more closely resembles that of the amorphous iron phosphate rather than that of Fe-free struvite, based on comparison with reference compounds. These observations indicate a transition from a crystalline magnesium phosphate lattice to a disordered iron-phosphate network.

As shown in Fig. 6b, the Fe L-edge spectra exhibit two prominent peaks arising from spin–orbit splitting: the L_3-edge at approximately 708.9 eV and the L_2-edge at 721.6 eV. The peak positions and characteristic splitting of the L_3 edge in the Fe-struvite microcrystals closely match those observed for the amorphous iron phosphate in the trivalent Fe(III) state. Although spectral analysis using the method[30] based on comparison of L_2 and L_3 peak heights in the XANES spectra, a small, albeit systematic, increase of the Fe(II) feature with increasing iron content is observed in comparison with monoclinic $FePO_4\cdot 2H_2O$ spectrum, based on the current solution chemistry, the formation of Fe(II) is unlikely. These results indicate a concentration-dependent Fe speciation mechanism: at low Fe^{3+} precursor concentrations (<10 ppm), iron is incorporated into the struvite lattice, whereas higher Fe^{3+} concentrations promote precipitation of a secondary amorphous Fe(III) phosphate phase. The amorphous nature of the iron phosphate phase is supported by XRD, and the presence of the phosphate pre-edge feature in XANES is consistent with previous reports.[62]

3.5 Confocal Raman spectromicroscopy of Fe-struvite microcrystals

Fe-struvite microcrystals were examined using an optical microscope to assess morphological changes as a function of Fe^{3+} concentration. As shown in Fig. 7a, Fe-free struvite consists of colorless needle-like microcrystals with average lengths and widths of approximately 12 and 1 μm, respectively. Upon addition of 10 ppm Fe^{3+}, the needles developed a reddish-brown tint, which intensified progressively with increasing Fe^{3+} concentration. This color change likely arises from Fe^{3+}-rich surface layers or finely dispersed secondary phases decorating the struvite needles. At 100 ppm Fe^{3+}, the needles exhibit stronger coloration, a noticeable reduction in length for many particles, and a more non-uniform size distribution. In the 200 ppm Fe-struvite sample, well-defined crystalline needles become markedly less abundant, while irregular, amorphous grains dominate. The amorphous character of these solids is consistent with the XRD results shown in Fig. 4a, confirming progressive suppression of long-range crystalline order with increasing Fe^{3+}content. At 500 ppm Fe^{3+}, the particle morphology is fully transformed: discrete struvite needles are rarely observed, and the precipitate consists primarily of dense, highly colored aggregates with a heterogeneous particle size distribution. The intense reddish-orange appearance reflects the presence of abundant Fe-rich phases, while the loss of a distinct crystal habit indicates that struvite formation is largely inhibited at this concentration. Overall, this systematic evolution from well-formed needles to amorphous Fe-rich aggregates highlights the strong influence of Fe^{3+} concentration on struvite nucleation and growth.

The size distribution of struvite microcrystals was evaluated at different Fe^{3+} concentrations, as illustrated in Fig. 7b. Fe-free

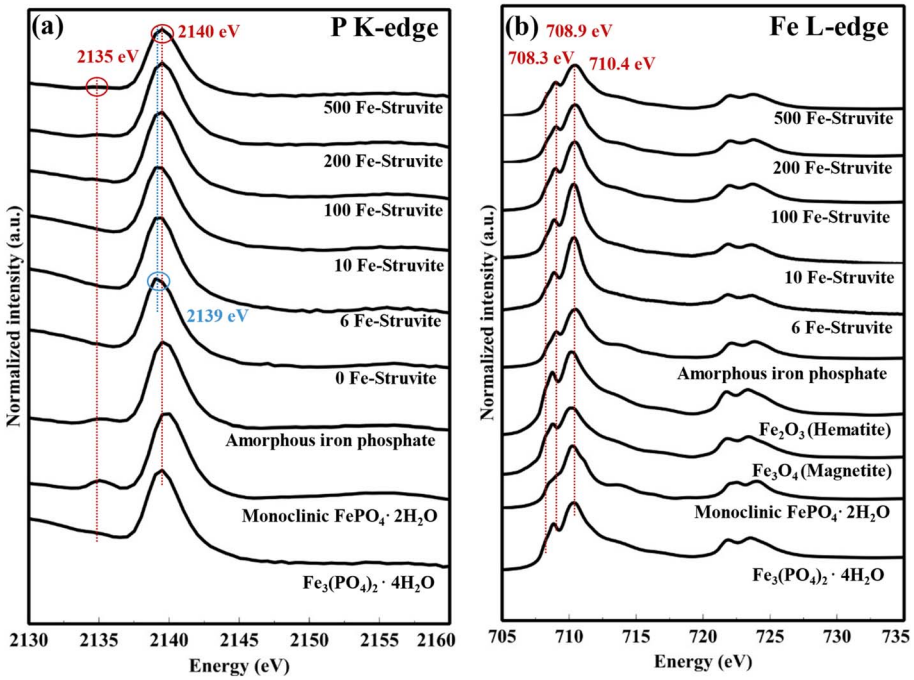

Fig. 6 XANES spectra of (a) P K-edge (b) Fe L-edge recorded for Fe-struvite microcrystals and selected reference materials.

struvite displays a narrow distribution with a well-defined maximum, corresponding to elongated needle-like microcrystals with average widths and lengths of approximately 1.2 μm and 12.3 μm, respectively. Upon the introduction of 10 ppm Fe^{3+}, the distribution becomes slightly broader and the main peak shifts towards higher values, with an average length of

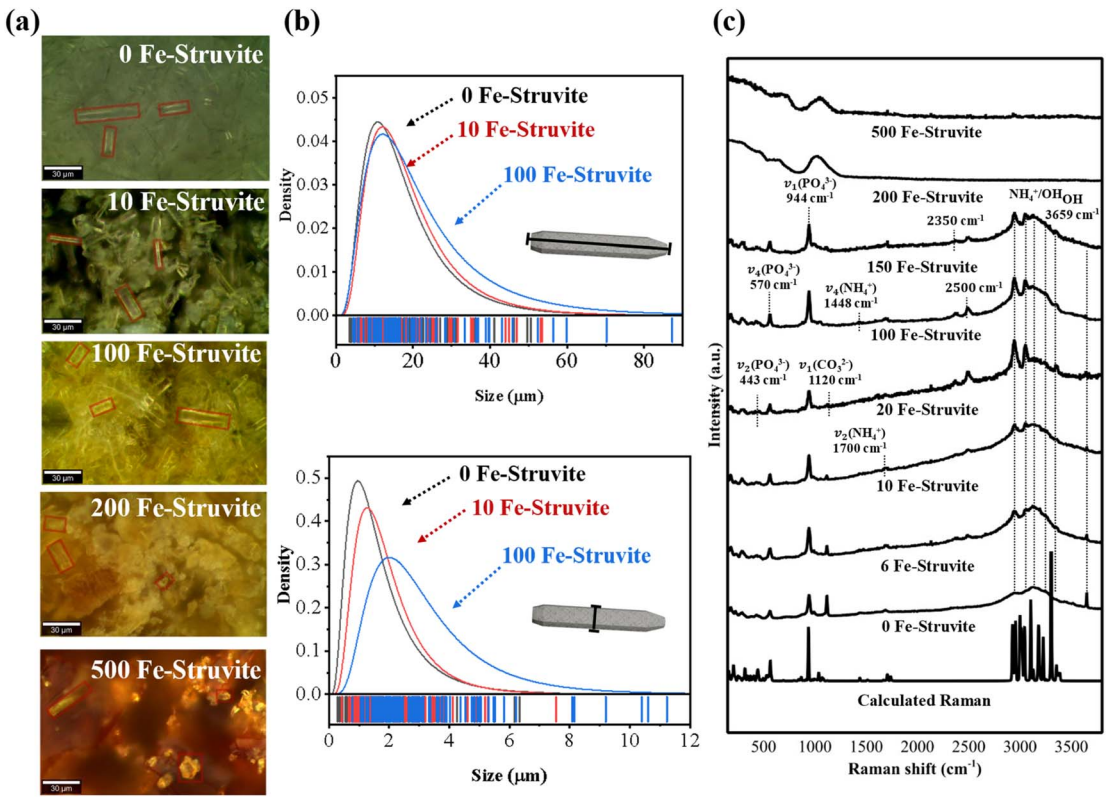

Fig. 7 (a) Optical micrographs of Fe-free and 10–500 ppm Fe-struvite, (b) their particle size distribution, and (c) the Raman spectra for struvite microcrystals synthesized using 0, 6, 10, 20, 100, 150, 200, and 500 ppm of Fe^{3+}.

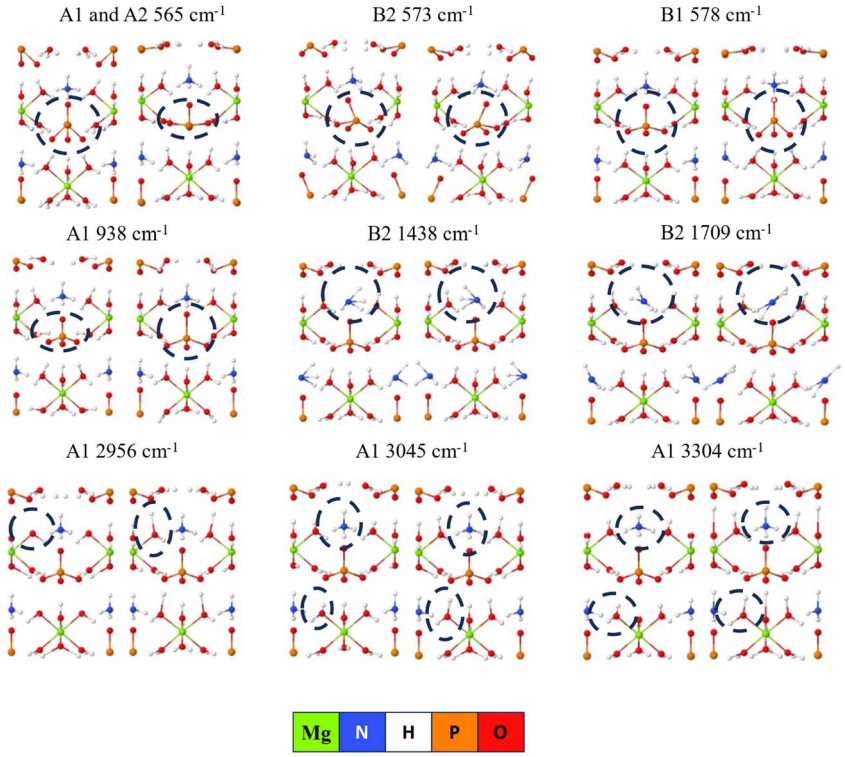

Fig. 8 Raman vibrational modes and their associated symmetry of crystalline struvite calculated using PBEsol0 hybrid functional and triple zeta quality polarized basis set. The dashed lines refer to the main vibrating molecules corresponding to the mentioned wavenumber.

around 13 μm. Increasing the Fe^{3+} concentration to 100 ppm further accentuated this shift, with the distribution progressively moving toward larger dimensions as amorphous grains with a wider size spread emerge, reaching ~2.1 and ~15 μm in width and length, respectively. This broadening reflects the coexistence of shortened struvite needles and larger, non-crystalline aggregates that dominate at higher Fe^{3+} levels. As Fe content increases, the contribution from well-defined needle-like particles diminishes, and the size distribution becomes increasingly governed by the amorphous fraction, consistent with the optical microscopy observations and the reduced crystallinity indicated by XRD (Fig. 4a).

Raman spectromicroscopy was employed to investigate changes in vibrational features of Fe-struvite. As shown in Fig. 7c, the spectrum of Fe-free struvite exhibits intense, well-defined peaks that closely match the calculated spectrum of pure struvite, including the symmetric phosphate stretching mode $\nu_1(PO_4^{3-})$ at 944 cm^{-1}.[63] The phosphate bending modes $\nu_2(PO_4^{3-})$ and $\nu_4{}^{-}PO_4^{3-}$) were observed at 443 and 570 cm^{-1}, respectively. Additionally, the $\nu_4(NH_4^{+})$ and $\nu_2(NH_4^{+})$ bending modes were detected at 1448 cm^{-1} and 1700 cm^{-1}, respectively.[20,64] Stretching modes of water molecules and ammonium ions were observed in the 2900–3700 cm^{-1} region.[64] A minor peak at 1120 cm^{-1}, assigned to the $\nu_1(CO_3^{2-})$ mode, was tentatively attributed to magnesium carbonate.[65] Addition of low Fe^{3+} concentrations (<20 ppm) did not result in significant shifts of the characteristic Raman bands, indicating that the local coordination environments of phosphate and ammonium groups remain largely unperturbed.

The intensity of the carbonate band decreased with increasing iron content, consistent with XRD results, likely due to the acidifying effect of the iron nitrate solution, which promotes dissolution of magnesium carbonate (hydromagnesite). Additional evidence for hydromagnesite reduction is provided by the attenuation of the sharp band at ~3659 cm^{-1}, attributed to OH^- groups on hydromagnesite surfaces associated with surface defects.[66] With increasing iron concentration, two new bands emerged at approximately 2350 and 2500 cm^{-1}, accompanied by rearrangement of NH_4^+ peak intensities in the 2800–3000 cm^{-1} region. Similar combination modes, such as $\nu_2(NH_4^{+})$ libration modes, have been reported for ammonium carbonate salts in the 2200–2500 cm^{-1} region.[67] A pronounced spectroscopic transition occurs at higher Fe^{3+} concentrations. In the 200 ppm Fe-struvite sample, and more prominently in the 500 ppm Fe-struvite sample, the sharp vibrational features characteristic of crystalline struvite are substantially attenuated and broadened. This loss of distinct vibrational modes reflects the disruption of long-range order and the transition to an amorphous phase.

To aid interpretation of the experimental Raman spectra, the DFT-calculated spectrum is shown in Fig. 8. The Raman-active modes are displayed to confirm the characteristic vibrational features of struvite, including phosphate, ammonium, and water-molecule vibrations. The mode at 570 cm^{-1} can be assigned to a bending vibration of the phosphate group (PO_4^{3-}).

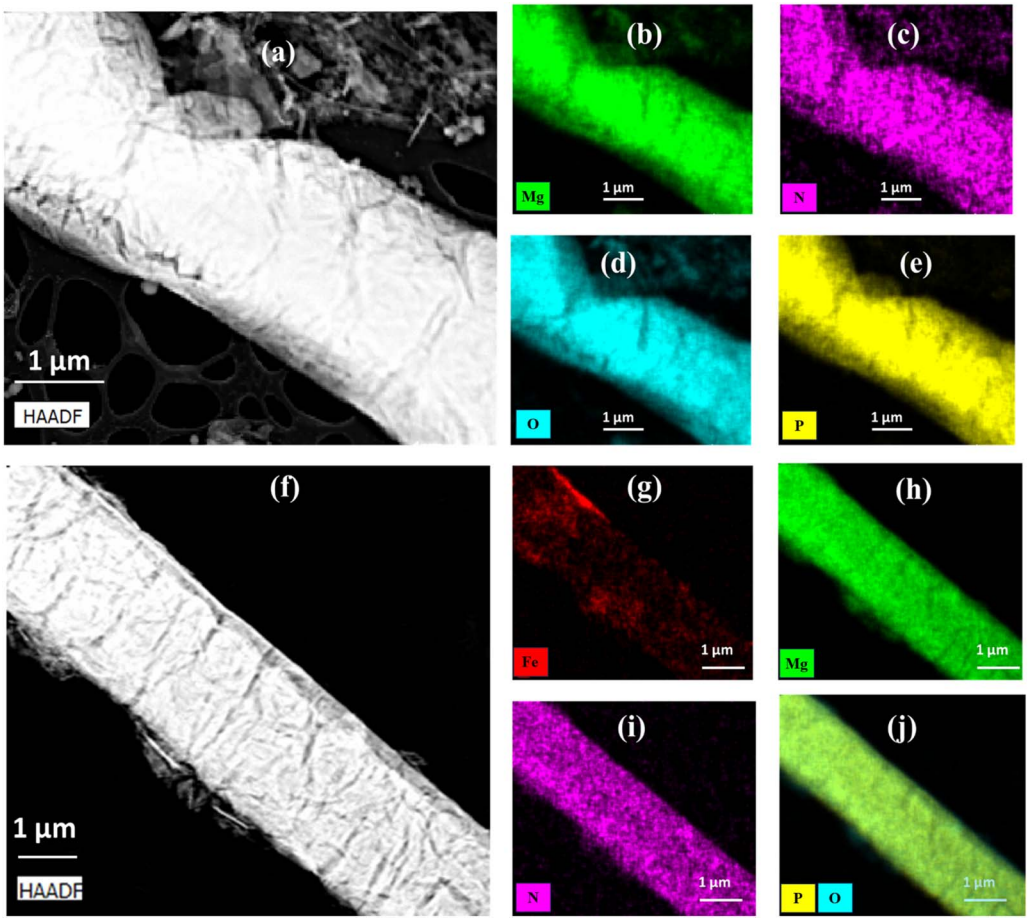

Fig. 9 (a–e) STEM images and the corresponding EDX elemental maps of Fe-free struvite and (f–j) 10 ppm Fe-struvite.

In the ideal T_d symmetry of a free phosphate ion, vibration corresponds to a single, triply degenerate asymmetric bending mode (F_2).[68,69] However, within the struvite lattice, symmetry is reduced to the site group (C_s), lifting the degeneracy, while and factor-group symmetry (C_{2v}), further splits the mode.[68,69] Fig. 8 illustrates this effect by resolving the ν_4 mode into a complex multiplet. Specifically, two vibrations belonging to A_1 (565.6 cm^{-1}) and A_2 (565.0 cm^{-1}) symmetry species appear as a single band because of their nearly identical energies, followed by the B_2 species at 573 cm^{-1} and the B_1 species at 578 cm^{-1}. This behavior is consistent with group theory predictions, which indicate that the coupled ν_4 vibrations should contain a complete set of Raman-active components (A_1, A_2, B_1, and B_2) in this region.[68] The experimental peak observed at 570 cm^{-1} therefore represents a convolution of these closely spaced lattice modes. The most intense calculated band appears at 938 cm^{-1} with A_1 symmetry and corresponds to the totally symmetric phosphate stretching mode $\nu_1(PO_4^{3-})$, validating the assignment of the strongest experimental peak observed at 944 cm^{-1}.

The ammonium (NH_4^+) group exhibits calculated B_2 symmetry modes at 1438 cm^{-1} and 1709 cm^{-1}, corresponding to H–N–H bending vibrations, in good agreement with the experimental bands at 1448 cm^{-1} and 1700 cm^{-1}. At higher frequencies, several stretching modes are predicted at 2956 cm^{-1}, 3045 cm^{-1}, and 3304 cm^{-1}, all with A_1 symmetry. This spectral region is dominated by O–H and N–H stretching vibrations, reflecting hydrogen bonding interactions involving lattice water molecules and ammonium ions. Notably, the Raman band at 1120 cm^{-1} observed experimentally is absent in the calculated struvite spectrum, indicating a non-PO_4^{3-} origin and supporting its assignment to carbonate species. Similarly, the doublet observed at ~2300 and ~2500 cm^{-1} in Fig. 7c is not present in the calculated spectrum, suggesting that it is a fingerprint of an iron phosphate-related phase. Although recent Raman studies of iron phosphate materials do not exhibit features in this spectral region [65], Fig. 8 indicates that the band at 2956 cm^{-1} is associated with Mg-coordinated H_2O stretching modes. We therefore tentatively propose that the bands observed at 2300–2500 cm^{-1}, arise from H_2O or NH_4^+ species adjacent to Fe centers or lattice vacancies, occupying a local coordination environment, distinct from that of crystalline struvite.

3.6 Morphological and elemental mapping investigation for Fe-free struvite and 10 ppm Fe-struvite

The morphological evolution of Fe-struvite microcrystals was investigated using HAADF-STEM. As shown in Fig. 9a,

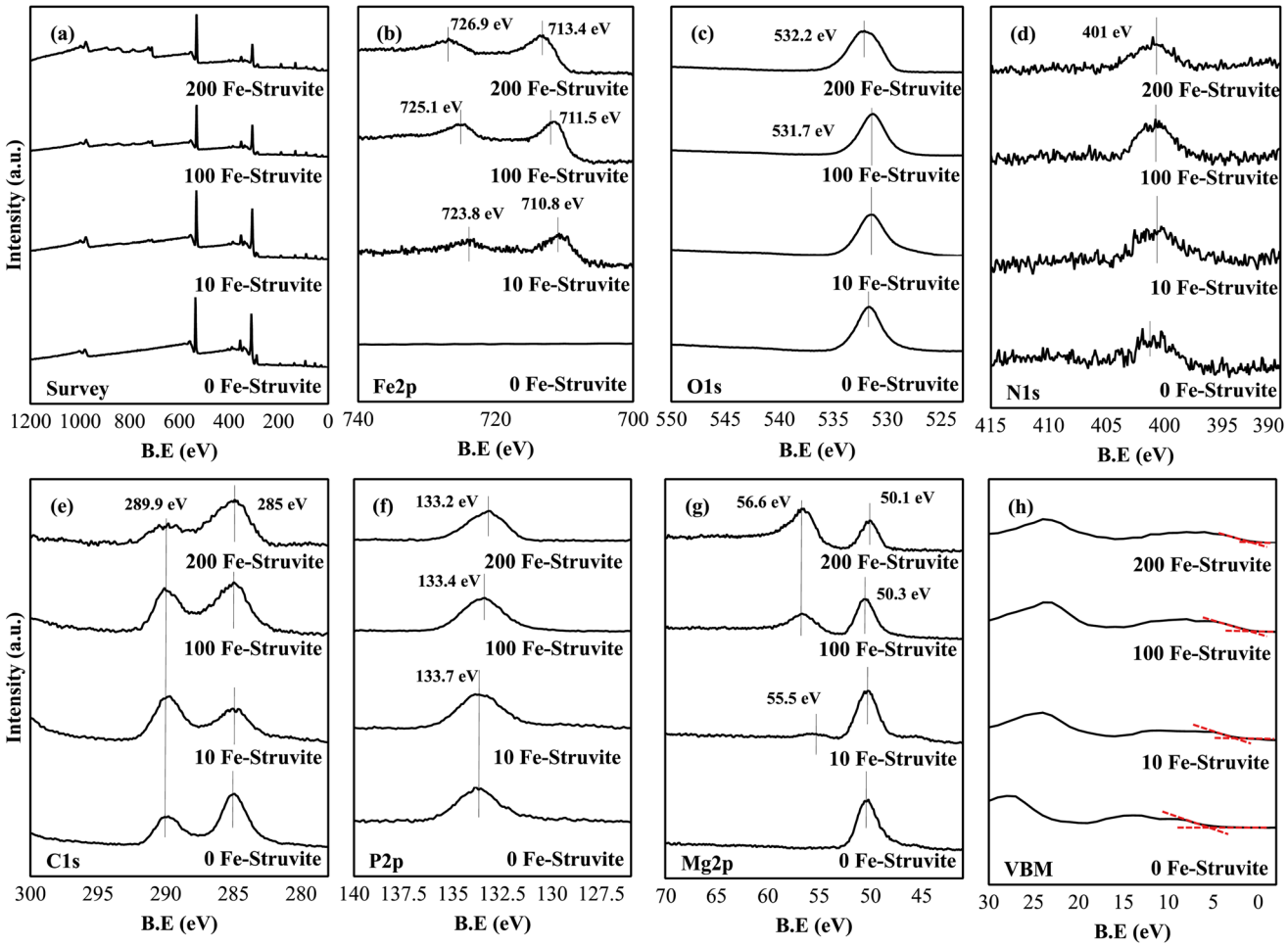

Fig. 10 XPS spectra of (a) survey, (b) Fe 2p, (c) O 1s, (d) N 1s, (e) C 1s, (f) P 2p, (g) Mg 2p, and (h) valence band.

elongated, needle-like microcrystals with well-defined facets are observed. Closer inspection of the HAADF contrast reveals subtle textural imperfections, such as surface rugosity and cracks. Despite these localized irregularities, the overall habit remains characteristic of highly crystalline struvite. Energy-dispersive X-ray (EDX) spectroscopy elemental mapping (Fig. 9b–e) shows a homogeneous spatial distribution of Mg, N, O, and P, confirming uniform co-localization of these elements within the crystalline lattice. It is also observed that the nitrogen signal appears weaker relative to the other elements. Upon introducing 10 ppm Fe^{3+} (Fig. 9f–j), the needle-like morphology is preserved, with no visible signs of amorphization, fragmentation, or significant surface roughening compared to Fe-free struvite. This persistence of morphology suggests that the crystallization mechanism remains largely unchanged at this impurity level. The Mg, N, O, and P elemental maps remain intense and spatially consistent with the microcrystal morphology, indicating that the bulk struvite phase is retained. In contrast, the iron distribution map (Fig. 9g) exhibits a weak and spatially sparse signal scattered across the microcrystal surface rather than a continuous or concentrated distribution. This disparity between the Fe signal and those of Mg or P indicates that iron is present only as a trace component, dispersed within the crystalline struvite matrix, rather than forming a distinct secondary phase.

3.7 Surface properties of Fe-struvite obtained *via* XPS analysis

The survey spectra shown in Fig. 10a displays peaks corresponding to Fe, O, N, C, P, and Mg corresponding to Fe-free, 10, 100, 200 ppm Fe-struvite. The high-resolution Fe 2p spectra of Fe-struvite in Fig. 10b reveals a characteristic doublet with Fe 2p3/2 and Fe 2p1/2 peak at 713.4 and 726.9 eV, respectively. These peaks are blue-shifted in 200 ppm Fe-struvite relative to those in 10 ppm Fe-struvite, indicating stronger iron bonding at higher Fe concentrations. The O 1s spectra in Fig. 10c exhibits a positive binding energy shift from 531.7 eV in Fe-free struvite to 532.2 eV in 200 ppm Fe-struvite, consistent with the trend observed for iron and indicating a complex reconfiguration of the oxygen coordination environments, where the formation of Fe–O–P networks might cause alteration to the overall balance of unresolved oxygen states within the peak envelope. The N 1s appears at ~401 eV and shows no measurable shift with increasing iron concentration (Fig. 10d). The C 1s spectrum in

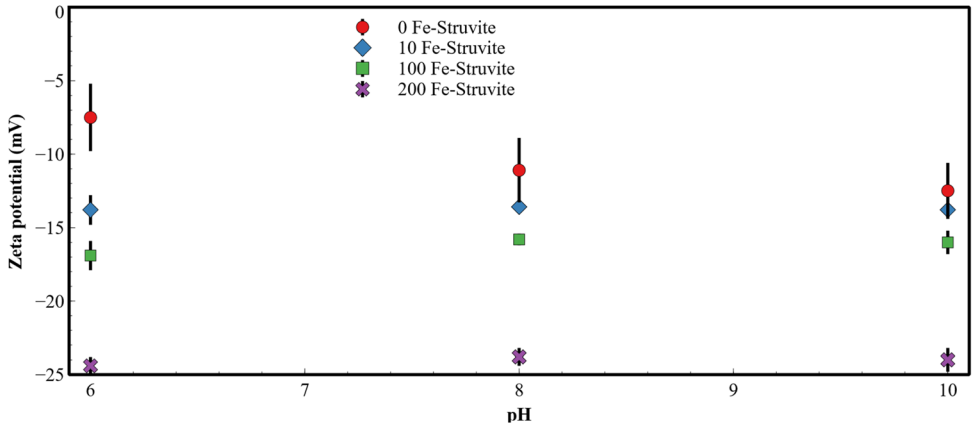

Fig. 11 Zeta potential for various Fe-struvite microcrystals.

Fig. 10e exhibits a peak at 289.9 eV, which is assigned to carbonate, while peak at 285 eV is for adventitious carbon.[70]

At higher Fe concentrations, the intensity of this carbonate-related peak decreases, consistent with progressive dissolution and loss of residual magnesium carbonate, in agreement with XRD and Raman results. The P 2p spectra in Fig. 10f show a peak at ~133.7 eV with no significant binding energy shift, indicating that the local electronic environment of phosphorus remains relatively unchanged. In Fig. 10g, a single Mg 2p peak is observed at 50.3 eV, while an additional peak at ~55.5 eV corresponding to Fe 3p emerges with increasing Fe^{3+} concentration. Fe 3p peak shifts to higher binding energy (from 55.5 to 56.6 eV) as Fe content increases, indicating increased electron deficiency of iron due to stronger chemical bonding, consistent with Fe–O–P linkage formation. In contrast, the Mg 2p peak exhibits a slight negative shift to lower binding energy (from 50.3 eV to 50.1 eV). This red shift suggests increased electron density around Mg^{2+} relative to Fe-free struvite, which can be interpreted as an electronic signature of competitive phosphate scavenging by Fe^{3+}. Because Fe^{3+} has a higher affinity for phosphate than Mg^{2+}, iron preferentially binds phosphate ligands,[71] weakening Mg-phosphate interactions and leaving Mg in a less polarizing coordination environment.

Iron incorporation also modifies the electronic structure, as reflected in the valence-band maximum (VBM) region shown in Fig. 10h. Fe-free struvite exhibits a wide band gap, with the valence-band edge located approximately 5 eV below the Fermi level ($E_F = 0$). H With increasing Fe content, the VBM shifts progressively toward E_F, reaching ~2 eV for 10 ppm Fe-struvite, 1 eV for 100 ppm Fe-struvite, and 0.5 eV for 200 ppm Fe-struvite microcrystals. The observed peak narrowing indicates the emergence of localized Fe 3d impurity states within the original band gap of insulating struvite.

3.8 Fe-struvite surface charge properties

Zeta potential measurements were performed in a 10 mM NaCl solution to control ionic strength, and the results are shown in Fig. 11. Fe-free struvite exhibits a negative or near-neutral surface charge, with values ranging from −5 mV to −12 mV. These values are consistent with previous literature reports of −8.2 to −16.5 mV at the same ionic strength.[72] It is further observed that incorporation of iron into the struvite structure induces a systematic shift toward most negative values, reaching approximately −25 mV. This pronounced increase in surface electronegativity provides direct interfacial evidence supporting the phase-segregation mechanism inferred from the XRF analysis. As the material transitions from a magnesium-dominated microcrystals to an iron-rich amorphous composite, surface chemistry becomes dominated by the iron (oxy)hydroxide and iron phosphate domains. These amorphous phases are enriched in surface hydroxyl groups (Fe–OH and P–OH), which undergo deprotonation ($Fe-OH \rightarrow Fe-O^- + H^+$) under the investigated pH conditions (pH 6–10). This process generates a high density of negatively charged surface sites ($Fe-O^-$), leading to the observed shift toward −25 mV even in the presence of 10 mM NaCl. Collectively, these results indicate that the outer surface of particles is no longer composed of struvite but is instead dominated by an iron-rich secondary phase.

4 Conclusions

Synthesis of Fe-struvite using the $MgCO_3$ chemical precipitation method produces microcrystals with complex structural characteristics that depend strongly on the Fe^{3+} precursor concentration. At low concentrations (up to 10 ppm), Fe^{3+} undergoes aliovalent substitution for Mg^{2+} within the struvite lattice, as evidenced by systematic XRD peak shifts. Increasing Fe^{3+} concentration also promotes dissolution of residual hydromagnesite, as demonstrated by Raman spectromicroscopy and XRD phase analysis. At higher Fe^{3+} loadings (>150 ppm), the crystalline struvite is no longer observed; the long-range order collapses, and an amorphous iron-phosphate matrix forms with a bulk stoichiometric Fe : P ratio of approximately 1 : 1.75. Perturbations in the local coordination environment of NH_4^+ and lattice H_2O molecules were inferred from Raman spectroscopy data. In particular, two peaks at 2350 and 2500 cm^{-1} appeared, which were assigned to be associated with Fe-centers of lattice vacancies. XPS surface analysis indicated important electronic effects taking place with the increasing Fe^{3+}

precursor concentration, especially prominent at 10 Fe-struvite, showing dispersed interactions lacking electron-withdrawing ability. A shift in valence band position by 2 eV was also observed from pure struvite to 10 Fe-struvite, indicating a significant hybridization of Fe 3d states within struvite. Hence, this integration of iron ions into the wide-bandgap struvite matrix fundamentally altered the local electronic structure. Consequently, this chemical restructuring is anticipated to induce significant shifts in the optical absorption profile and create novel surface active sites that may become active in the environment. Therefore, future studies will focus on evaluating the optical and photocatalytic properties and reactivity of Fe-struvite in environmentally relevant solutions. In addition, investigating the stability and solubility of these Fe-struvite microcrystals is essential to assess their metal release properties.

Author contributions

Conceptualization: S. H. and J. B.; methodology: S. H. and J. B.; formal analysis: S. H., S. M. K. H. F (XANES and XRF analysis), and P. E. (kinetic modeling); investigation: S. H. (synthesis, analysis and characterization), M. S. (XANES data acquisition), D. T. A. (XRD measurements), M. A. (XPS measurements), and L. Z. (STEM imaging); resources: J. B. and A. L.; writing – original draft: S. H.; writing – review & editing: S. H., C. S., A. L., and J. B.; supervision: J. B.; funding acquisition: J. B. and A. L.

All authors have read and agreed to the published version of the manuscript.

Conflicts of interest

The authors declare no conflicts of interest.

Data availability

All data supporting the findings of this study are available from the corresponding author upon reasonable request.

Acknowledgements

We acknowledge support from the National Science Foundation collaborative research grants (awards CHE-2404150, Purdue University group; CHE-2404151, Lehigh University). TEM characterization was conducted as part of a user project GUP-318041 at the Center for Nanophase Materials Sciences (CNMS), which is a US Department of Energy, Office of Science User Facility at Oak Ridge National Laboratory. In addition, this work was carried out with the support of Diamond Light Source, instrument B07B (proposal cm40617).

References

1 X. Hao, J. Li, R. Liu and M. C. M. van Loosdrecht, *Environ. Sci. Technol.*, 2024, **58**, 14065–14067.
2 A. Kogler, M. Farmer, J. A. Simon, S. Tilmans, G. F. Wells and W. A. Tarpeh, *ACS ES&T Eng.*, 2021, **1**, 662–684.
3 K. Solon, E. I. P. Volcke, M. Spérandio and M. C. M. Van Loosdrecht, *Environ. Sci.: Water Res. Technol.*, 2019, **5**, 631–642.
4 X. Chen, Y. Gao, D. Hou, H. Ma, L. Lu, D. Sun, X. Zhang, P. Liang, X. Huang and Z. J. Ren, *Environ. Sci. Technol. Lett.*, 2017, **4**, 305–310.
5 M. N. Nadagouda, G. Varshney, V. Varshney and C. A. Hejase, *ACS Environ. Au*, 2024, **4**, 271–291.
6 P. Wilfert, P. S. Kumar, L. Korving, G.-J. Witkamp and M. C. M. Van Loosdrecht, *Environ. Sci. Technol.*, 2015, **49**, 9400–9414.
7 M. A. Butkus, D. Grasso, C. P. Schulthess and H. Wijnja, *J. Environ. Qual.*, 1998, **27**, 1055–1063.
8 H. Yan and K. Shih, *Water Res.*, 2016, **95**, 310–318.
9 B. D. Shoener, I. M. Bradley, R. D. Cusick and J. S. Guest, *Environ. Sci.: Processes Impacts*, 2014, **16**, 1204–1222.
10 H. Gao, Y. D. Scherson and G. F. Wells, *Environ. Sci.: Processes Impacts*, 2014, **16**, 1223–1246.
11 J. A. O'Neal and T. H. Boyer, *Environ. Sci.: Water Res. Technol.*, 2015, **1**, 481–492.
12 D. Maddewor, P. Kemacheevakul, N. Phungsombun, P. Savatdipap and S. Chuangchote, *Environ. Sci.: Water Res. Technol.*, 2024, **10**, 2230–2242.
13 Q. Wang, H. Jung, B. Wan, P. Liu, P. Yang and Y. Tang, *ACS Sustain. Chem. Eng.*, 2021, **9**, 10630–10641.
14 Q. Wang, C. Zhang, D. Patel, H. Jung, P. Liu, B. Wan, S. G. Pavlostathis and Y. Tang, *Environ. Sci. Technol.*, 2020, **54**, 8362–8372.
15 Q. Wang, X. Liu, H. Jung, S. Zhao, S. G. Pavlostathis and Y. Tang, *ACS Sustain. Chem. Eng.*, 2021, **9**, 9093–9105.
16 Q. Guan, G. Zeng, B. Gong, Y. Li, H. Ji, J. Zhang, J. Song, C. Liu, Z. Wang and C. Deng, *J. Clean. Prod.*, 2021, **328**, 129588.
17 Y. Pinatha, C. Polprasert and A. J. Englande, *Sci. Total Environ.*, 2020, **713**, 136514.
18 K. P. Fattah, S. Sinno, S. Atabay, Z. Khan, Z. Al-Dawood, A. K. Yasser and R. Temam, *Energies*, 2022, **15**, 4585.
19 B. Lu, D. Kiani, W. Taifan, D. Barauskas, K. Honer, L. Zhang and J. Baltrusaitis, *J. Phys. Chem. C*, 2019, **123**, 8908–8922.
20 E. Kirinovic, A. R. Leichtfuss, C. Navizaga, H. Zhang, J. D. Schuttlefield Christus and J. Baltrusaitis, *ACS Sustain. Chem. Eng.*, 2017, **5**, 1567–1577.
21 W. A. Deer, R. A. Howie and J. Zussman, *An Introduction to the Rock-Forming Minerals*, Mineralogical Society of Great Britain and Ireland, London, 2013.
22 P. W. Scott and C. M. Bristow, *Industrial Minerals and Extractive Industry Geology*, Geological Society, London, 2002.
23 M. Silva, V. Murzin, L. Zhang, J. Baltrus and J. Baltrusaitis, *Environ. Sci.:Nano*, 2020, **7**, 3482–3496.
24 D. Xu, X. Xiong, L. Yang, Z. Zhang and X. Wang, *J. Chem. Eng. Data*, 2016, **61**, 78–82.
25 Q. Gautier, P. Bénézeth, V. Mavromatis and J. Schott, *Geochim. Cosmochim. Acta*, 2014, **138**, 1–20.
26 A. Capdevielle, E. Sýkorová, B. Biscans, F. Béline and M.-L. Daumer, *J. Hazard. Mater.*, 2013, **244–245**, 357–369.

27 F. Abbona, M. Calleri and G. Ivaldi, *Acta Crystallogr., Sect. B:Struct. Sci.*, 1984, **40**, 223–227.
28 M. Akao and S. Iwai, *Acta Crystallogr., Sect. B: Struct. Sci.*, 1977, **33**, 1273–1275.
29 D. C. Grinter, P. Ferrer, F. Venturini, M. A. van Spronsen, A. I. Large, S. Kumar, M. Jaugstetter, A. Iordachescu, A. Watts and S. L. M. Schroeder, *J. Synchrotron Radiat.*, 2024, **31**, 578–589.
30 R. C. Moffet, H. Furutani, T. C. Rödel, T. R. Henn, P. O. Sprau, A. Laskin, M. Uematsu and M. K. Gilles, *J. Geophys. Res.:Atmos.*, 2012, **117**, D07204.
31 D. E. Latta, A. Neumann, W. Premaratne and M. M. Scherer, *ACS Earth Space Chem.*, 2017, **1**, 197–208.
32 H. Tamura, K. Goto, T. Yotsuyanagi and M. Nagayama, *Talanta*, 1974, **21**, 314–318.
33 J. H. Scofield, *J. Electron Spectrosc. Relat. Phenom.*, 1976, **8**, 129–137.
34 D. A. Shirley, *Phys. Rev. B*, 1972, **5**, 4709.
35 N. Fairley, V. Fernandez, M. Richard-Plouet, C. Guillot-Deudon, J. Walton, E. Smith, D. Flahaut, M. Greiner, M. Biesinger and S. Tougaard, *Appl. Surf. Sci. Adv.*, 2021, **5**, 100112.
36 A. Erba, J. K. Desmarais, S. Casassa, B. Civalleri, L. Donà, I. J. Bush, B. Searle, L. Maschio, L. Edith-Daga and A. Cossard, *J. Chem. Theory Comput.*, 2022, **19**, 6891–6932.
37 S. Grimme, J. Antony, S. Ehrlich and H. Krieg, *J. Chem. Phys.*, 2010, **132**, 154104.
38 S. Grimme, S. Ehrlich and L. Goerigk, *J. Comput. Chem.*, 2011, **32**, 1456–1465.
39 D. Vilela Oliveira, J. Laun, M. F. Peintinger and T. Bredow, *J. Comput. Chem.*, 2019, **40**, 2364–2376.
40 L. Maschio, B. Kirtman, R. Orlando and M. Rèrat, *J. Chem. Phys.*, 2012, **137**, 204113.
41 C. M. Zicovich-Wilson, F. Pascale, C. Roetti, V. R. Saunders, R. Orlando and R. Dovesi, *J. Comput. Chem.*, 2004, **25**, 1873–1881.
42 F. Pascale, C. M. Zicovich-Wilson, F. López Gejo, B. Civalleri, R. Orlando and R. Dovesi, *J. Comput. Chem.*, 2004, **25**, 888–897.
43 G. Ferraris, H. Fuess and W. Joswig, *Acta Crystallogr., Sect. B: Struct. Sci.*, 1986, **42**, 253–258.
44 N. Ma and A. A. Rouff, *Environ. Sci. Technol.*, 2012, **46**, 8791–8798.
45 A. Paskin, T. Couasnon, J. P. H. Perez, S. S. Lobanov, R. Blukis, S. Reinsch and L. G. Benning, *J. Am. Chem. Soc.*, 2023, **145**, 15137–15151.
46 S. M. El-Sayed, T. M. Meaz, M. A. Amer and H. A. El Shersaby, *Part. Sci. Technol.*, 2014, **32**, 39–45.
47 U. K. Wadne, R. H. Kadam, K. M. Batoo, M. L. Mane, S. Hussain, S. E. Shirsath and A. R. Shitre, *Ceram. Int.*, 2023, **49**, 8132–8139.
48 S. I. Shah, W. Li, C.-P. Huang, O. Jung and C. Ni, *Proc. Natl. Acad. Sci. U. S. A.*, 2002, **99**, 6482–6486.
49 D.-M. Kim, S. C. Jung, S. Ha, Y. Kim, Y. Park, J. H. Ryu, Y.-K. Han and K. T. Lee, *Chem. Mater.*, 2018, **30**, 3199–3203.
50 W. Hume-Rothery, G. Mabbott W and K. M. Channel Evans, *Philos. Trans. R. Soc., A*, 1934, **233**, 1–97.
51 S. Boudin and K.-H. Lii, *Inorg. Chem.*, 1998, **37**, 799–803.
52 Y. Miao, Y. Zhao, S. Zhang, R. Shi and T. Zhang, *Adv. Mater.*, 2022, **34**, 2200868.
53 A. Whitaker and J. W. Jeffery, *Acta Crystallogr., Sect. B: Struct. Sci.*, 1970, **26**, 1429–1440.
54 S. Lu, P. Yan, Y. Gao and C. Zhang, *Cryst. Growth Des.*, 2020, **20**, 3722–3731.
55 H. Huang, D. Zhang, W. Wang, B. Li, N. Zhao, J. Li and J. Dai, *Sci. Total Environ.*, 2019, **655**, 211–219.
56 C. K. Chauhan and M. J. Joshi, *J. Cryst. Growth*, 2014, **401**, 221–226.
57 K. Shih and H. Yan, in *Environmental Materials and Waste*, ed. M. N. V Prasad and K. Shih, Academic Press, Amsterdam, 2016, pp. 665–686.
58 M. Gargouri, C. Chtara, P. Charrock, A. Nzihou and H. El Feki, *J. Chem. Chem. Eng.*, 2010, **4**, 49–57.
59 M. Schultz, W. Burckhardt and S. T. Barth, *J. Mater. Sci.*, 1999, **34**, 2217–2227.
60 L. N. Plummer and T. M. L. Wigley, *Am. J. Sci.*, 1978, **278**, 179–216.
61 C. A. J. Appelo and D. Postma, *Geochemistry, Groundwater and Pollution*, CRC Press, Boca Raton, Florida, 2nd edn., 2005.
62 D. Hesterberg, W. Zhou, K. J. Hutchison, S. Beauchemin and D. E. Sayers, *J. Synchrotron Radiat.*, 1999, **6**, 636–638.
63 D. Kiani, M. Silva, Y. Sheng and J. Baltrusaitis, *J. Phys. Chem. C*, 2019, **123**, 25135–25145.
64 V. Stefov, B. Šoptrajanov, I. Kuzmanovski, H. D. Lutz and B. Engelen, *J. Mol. Struct.*, 2005, **752**, 60–67.
65 N. Buzgar and A. I. Apopei, *An. Ştiinţ. Univ. Al. I. Cuza Iaşi, Geol.*, 2009, **2**, 97–112.
66 W. W. Focke, D. Molefe, F. J. W. Labuschagne and S. Ramjee, *J. Mater. Sci.*, 2009, **44**, 6100–6109.
67 A. D. Fortes, I. G. Wood, D. Alfè, E. R. Hernández, M. J. Gutmann and H. A. Sparkes, *Acta Crystallogr., Sect. B: Struct. Sci.*, 2014, **70**, 948–962.
68 V. G. Koleva, *Spectrochim. Acta - A: Mol. Biomol. Spectrosc.*, 2007, **66**, 413–418.
69 S. C. B. Myneni, *Rev. Mineral. Geochem.*, 2000, **40**, 113–172.
70 R. Dedryvère, L. Gireaud, S. Grugeon, S. Laruelle, J.-M. Tarascon and D. Gonbeau, *J. Phys. Chem. B*, 2005, **109**, 15868–15875.
71 Y. Liu, X. Li, X. Yang, S. Chang, J. Feng, X. Li, X. Zhu, Y. Zong, X. Liu and X. Zheng, *J. Mater. Sci.: Mater. Electron.*, 2022, **33**, 5587–5598.
72 M. Fromberg, M. Pawlik and D. S. Mavinic, *Powder Technol.*, 2020, **360**, 715–730.